

INTRA-CLUSTER LIGHT AT THE FRONTIER: ABELL 2744

MIREIA MONTES^{1,2} AND IGNACIO TRUJILLO^{1,2}

¹Instituto de Astrofísica de Canarias, c/ Vía Láctea s/n, E38205 - La Laguna, Tenerife, Spain and

²Departamento de Astrofísica, Universidad de La Laguna, E38205 La Laguna, Tenerife, Spain

Draft version August 19, 2018

ABSTRACT

The ultra-deep multiwavelength HST Frontier Fields coverage of the Abell Cluster 2744 is used to derive the stellar population properties of its intra-cluster light (ICL). The restframe colors of the ICL of this intermediate redshift ($z = 0.3064$) massive cluster are bluer ($g - r = 0.68 \pm 0.04$; $i - J = 0.56 \pm 0.01$) than those found in the stellar populations of its main galaxy members ($g - r = 0.83 \pm 0.01$; $i - J = 0.75 \pm 0.01$). Based on these colors, we derive the following mean metallicity $Z = 0.018 \pm 0.007$ for the ICL. The ICL age is 6 ± 3 Gyr younger than the average age of the most massive galaxies of the cluster. The fraction of stellar mass in the ICL component comprises at least 6% of the total stellar mass of the galaxy cluster. Our data is consistent with a scenario where the bulk of the ICL of Abell 2744 has been formed relatively recently ($z < 1$). The stellar population properties of the ICL suggest that this diffuse component is mainly the result of the disruption of infalling galaxies with similar characteristics in mass ($M_{\star} \sim 3 \times 10^{10} M_{\odot}$) and metallicity than our own Milky Way. The amount of ICL mass in the central part of the cluster (< 400 kpc) is equivalent to the disruption of 4 – 6 Milky Way-type galaxies.

Subject headings: galaxies: clusters: individual (Abell 2744) — galaxies: evolution — galaxies: photometry — galaxies: halos

1. INTRODUCTION

A substantial fraction of stars in clusters are not gravitationally bound to any particular galaxy. These stars constitute the so-called intra-cluster light. The ICL is distributed around the central galaxy of the cluster and extends to several hundred kpc away from the cluster center (e.g. Murante et al. 2004; Zibetti et al. 2005). This diffuse light is thought to form primarily by the tidal stripping of stars from galaxies which interact and merge during the hierarchical accretion history of the cluster (e.g. Gregg & West. 1998; Rudick et al. 2006; Conroy et al. 2007; Contini et al. 2014). Therefore, the characterization of the ICL provides a direct way of determining the assembly mechanisms occurring inside galaxy clusters. In this sense, the ICL is the signature of how violent the assembly of the cluster has been through its cosmic history. For that reason, it is absolutely key determining how and when the ICL formed. However, the identification of this light observationally remains difficult and uncertain. Indeed, the typical surface brightness of the ICL is $\mu_V \gtrsim 26.5$ mag/arcsec² (e.g. Mihos et al. 2005; Zibetti et al. 2005; Rudick et al. 2006) and it is contaminated by foreground and background galaxies. Moreover, it is difficult to dissociate between the ICL and the brightest central galaxy surface brightness profile (e.g. Gonzalez et al. 2005; Krick et al. 2007).

Although the properties of the stellar populations of the ICL provide a vital tool to understand its formation, little is known about their characteristics. The ICL is reported to be metal-poor in some studies (e.g. Durrell et al. 2002; Williams et al. 2007) while other studies show super-solar metallicities (e.g. Krick et al. 2006). Simulations predict that the ICL forms very late ($z < 1$; e.g. Murante et al. 2007; Contini et al. 2014) and

that the bulk of the ICL is produced by the most massive ($M_{\star} \sim 10^{10-11} M_{\odot}$) satellites as they fall into the cluster core (e.g. Murante et al. 2007; Purcell et al. 2007; Martel et al. 2012; Contini et al. 2014). If this scenario is correct, the ages and metallicities of the intracluster population will be highly dependent on the progenitor galaxies from which they were stripped. Therefore, the ICL is expected to have a metallicity that is similar to that of these massive satellites. The goal of this paper is to explore this question in detail and characterize, for the first time, the age and metallicity of the ICL of a massive cluster at radial distances $R > 50$ kpc with unprecedented accuracy.

We achieve our goal taking advantage of the deepest optical and near-infrared images ever taken by the Hubble Space Telescope (*HST*) of the Abell Cluster 2744. The Hubble Frontier Fields¹ (HFF) project represents the largest investment of HST time for deep observations of galaxy clusters. Abell 2744 is the first cluster observed as part of the HFF program. This structure, at $z = 0.3064$ (Owers et al. 2011), is a rich cluster (virial mass of $\sim 7 \times 10^{15} M_{\odot}$ within $R < 3.7$ Mpc) undergoing a major merger as evidenced by its complex internal structure (Boschin et al. 2006). Therefore, this cluster represents an excellent target for studying the formation of the ICL. The ages and metallicities of the ICL are studied in detail taking advantage of the inclusion of very deep near-infrared (NIR) data to break the age-metallicity degeneracy (e.g. Anders et al. 2004).

Throughout this work, we adopt a standard cosmological model with the following parameters: $H_0 = 70$ km s⁻¹ Mpc⁻¹, $\Omega_m = 0.3$ and $\Omega_{\Lambda} = 0.7$. At $z = 0.3064$, this corresponds to a spatial scale of 4.52 kpc/arcsec.

email:mireia.montes.quiles@gmail.com

¹ <http://www.stsci.edu/hst/campaigns/frontier-fields>

2. DATA

The data used in this work are based on the first release of the HFF program and include all the NIR WFC3 data (ID13495, PI: J. Lotz and ID13386, PI: S. Rodney) of Abell 2744. The ACS images were taken from the HST archive as part of the program: ID11689 (PI: R. Dupke) and consist of six orbits in F435W and five orbits each in F606W and F814W. NIR observations include imaging in four filters F105W, F125W, F140W, F160W based on 24, 12, 10, and 24 orbits, respectively. The data were directly retrieved from the archive². The images were reduced by the HFF team following standard HST procedures both for the ACS and WFC3 data³. For both cameras, flat fields are claimed to be accurate to better than 1% across the detector. A few of the HFF observations in the IR exhibit a time-variable sky background signal due to time variable atmospheric emission. This exposures were corrected from this variable emission and included into the final mosaics (Koekemoer 2014, priv. comm.).

The mosaics we used consist of drizzled science images with pixel size $0''.06$. These mosaics were build using the package Astrodrizzle⁴. In the case of the WFC3, this pixel size is closer to one half of an original pixel. While working with subpixel dithered data has several advantages as helping to the cosmic ray rejection step, improving the resolution and lowering the correlated noise, it also reduces the sensitivity to low surface brightness features. This last problem, however, can be avoided by combining several pixels later on as we have done in our work (see next section).

The $0.4''$ diameter aperture depth at 5σ of each image is: 27.4 (F435W), 28.0 (F606W), 27.1 (F814W), 28.6 (F105W), 28.5 (F125W), 28.7 (F140W) and 28.2 (F160W) mag (Laporte et al. 2014). As we will explain later, the age and metallicity of the ICL is determined using the color information provided by both cameras: ACS and WFC3. Consequently, we will limit our study of the ICL to their common field of view ($\sim 2.0 \times 2.2$ arcmin²) of the galaxy cluster.

2.1. Surface brightness limits

Our goal is to study the properties of the stellar populations of Abell 2744 down to the faintest surface brightness possible. For this reason, it is necessary to measure accurately the colors of the stellar populations across the cluster. Given that the ACS images are shallower than the WFC3 data, we have spatially re-binned the images of the HFF to improve the S/N and to maximize the detection of the diffuse light of the cluster. Previous to the rebinning, we have smoothed the images with a 5 pixel median box filter to reduce noise, specially in the outer regions of the cluster. The new rebinned pixel value is the sum of 25 input pixels in the original image and has a size of $0.3''$ (~ 1.4 kpc at $z = 0.3064$). The process of smoothing and rebinning the images is flux conserving.

We have estimated the surface brightness limits of our images as follows. We have identified 20 background regions spread over the outer parts of the images. The

background regions are chosen to avoid the contamination of the light of the cluster. With this aim we have selected areas with $\mu_J > 28$ mag/arcsec², $\rho < 10^{0.7}$ M_⊙/pc² and $R > 230$ kpc (see Section 2.2). We have explored whether the light distribution in the background area follows a normal distribution. A Kolmogorov-Smirnov test indicates that a gaussian distribution is compatible with the data (the null hypothesis is not rejected with any statistical significance). We do not find any evidence supporting that our background distributions present gradients.

To estimate the surface brightness limits, we calculated the r.m.s of the images on boxes of 3×3 arcsec² (equivalent to 10×10 kpc² at the cluster redshift). The surface brightness limits we provide correspond to 3σ detections. These limits are: 29.31 ± 0.02 (F435W), 29.60 ± 0.10 (F606W), 29.13 ± 0.07 (F814W), 30.32 ± 0.08 (F105W), 29.97 ± 0.09 (F125W), 30.01 ± 0.05 (F140W) and 30.05 ± 0.03 (F160W) mag/arcsec². Although the HFF data is sky subtracted, in order to have a better sky determination, we have used the above regions to reestimate the background of each of the images and subtracted (added) it to the whole image.

Finally, for the analysis of the ICL, it is crucial to identify the galaxies that are members of the cluster and get rid of background and foreground sources. For this purpose, we build a redshift mask of the cluster image. The mask was constructed using the spectroscopic redshift catalog of Owers et al. (2011) and adding all the photometric redshifts available in NED⁵. To assign a redshift value to the pixels of the images, first we run SEXTRACTOR in the F160W image to identify the area that correspond to each object, using a detection threshold at a 5σ significance level and a gaussian convolution kernel with size $0.75''$. Then, we masked the area subtended by those objects whose redshifts do not correspond to the cluster ($z > 0.33$ and $z < 0.27$) and also those without measured redshifts.

2.1.1. Background level uncertainties

The uncertainties at determining the surface brightness limits of the images reflect how accurate we can estimate the background level. We have quantified how these uncertainties affect the determination of the fluxes in the ICL region of our images. As we will see later, we define the ICL as the region of the cluster with restframe surface brightness $24 < \mu_J < 25$ mag/arcsec². Placing in this region a 3×3 arcsec² box, we measured the flux in it. This ICL flux was then compared with the uncertainties at the determination of the background. We find that the previous background uncertainties translate into the following errors on the different bands fluxes in our ICL bin: 24% (F435W), 5.3% (F606W), 4.1% (F814W), 0.4% (F105W), 0.3% (F125W), 0.4% (F140W) and 0.1% (F160W). As expected, the errors are larger for our ACS filters, which have shallower exposures, than for our WFC3 filters. However, it is worth noting, that our work only uses data based on bands redder than F606W. Consequently, the uncertainties at measuring the background level only affect the fluxes in the ICL region below 5% in all cases. This little effect, particularly in the NIR bands, is ex-

² <http://www.stsci.edu/hst/campaigns/frontier-fields/FF-Data>

³ More details on the FF images reduction in: http://archive.stsci.edu/pub/hlsp/frontier/abell2744/images/hst/v1.0/hlsp_frontier_hst_wfc3-acs_abell2744_v1.0_readme.pdf

⁴ <http://drizzlepac.stsci.edu/>

⁵ <http://ned.ipac.caltech.edu/>

pected because our surface brightness limit to study the ICL is well above (~ 4 mag) the limiting surface brightness of our imaging. This guarantee that we are working in a surface brightness regime less affected by problems of flat fielding, incorrect sky subtraction, etc. In Table 1, we summarize the sources of noise that can affect our measurements.

2.2. Optical and NIR colors

In order to study the stellar populations of the cluster, including its ICL, we constructed two restframe colors at the redshift of the cluster: $g - r$ and $i - J$. The choice of these colors was made for two reasons: first, to diminish the effects of the different PSFs combining images from the same camera (ACS data for $g - r$ and WFC3 data for $i - J$) and second, to include a NIR filter to constrain the metallicity with better accuracy (e.g. Anders et al. 2004). The colors were built interpolating among the observed filters to obtain the flux in the equivalent restframe bands: g , r , i and J . We also derived the z band, using the same methodology, to construct the $r - z$ color. This color was used to create a measurement of the stellar mass density of the cluster (see below). We corrected our data of Galactic extinction ($E(B-V)=0.012$, Schlafly & Finkbeiner 2011) using a Cardelli et al. (1989) extinction law.

To explore the stellar populations of Abell 2744 and their variation across the cluster structure, we make use of three independent analysis based on different parameters: the restframe (corrected of cosmological dimming) surface brightness in J -band, μ_J , the logarithm of the stellar mass density, $\log(\rho)$, and the radial distance, R , to the most massive galaxies of the cluster. These three parameters will allow us to compare our results with theoretical expectations.

The μ_J map of the cluster was divided in eight surface brightness bins, from 16 to 25 mag/arcsec². To estimate $\log(\rho)$, we follow the procedure described in Bakos et al. (2008). First, we link the stellar mass density profile ρ with the surface brightness profile at a given wavelength μ_λ using the mass-to-light (M/L) ratio. This is done with the expression:

$$\log(\rho) = \log(M/L)_\lambda - 0.4(\mu_\lambda - m_{abs\odot\lambda}) + 8.629 \quad (1)$$

where $m_{abs\odot\lambda}$ is the absolute magnitude of the Sun at wavelength λ and ρ is measured in $M_\odot \text{ pc}^{-2}$. Second, to evaluate the above expression, we need to obtain the M/L ratio at each radius. Following the prescription of Bell et al. (2003), we have calculated the M/L ratio as a function of color. In this work we have used the restframe color $r - z$ and assumed a Salpeter IMF (Salpeter 1955). The expression we have used to estimate the M/L is:

$$\log(M/L)_\lambda = (a_\lambda + b_\lambda \times color) \quad (2)$$

where $color = r - z$, $a_\lambda = -0.041$ and $b_\lambda = 0.463$ are applied to determine the M/L in the z -band. The $\log(\rho)$ map of the cluster was divided also in eight mass density bins, from $10^{4.8}$ to $10^{0.8} M_\odot/\text{pc}^2$.

Finally, we constructed a *radial distance* indicator using the centers of the most massive galaxies in the cluster as the starting points. These massive galaxies were identified as those galaxies with central surface brightness

$\mu_J < 17$ mag/arcsec². This surface brightness translates to a density of $10^4 M_\odot/\text{pc}^2$ equivalent to the stellar mass densities in the centers of massive ellipticals (e.g. Hopkins et al. 2009). Then, the distance to their centers was calculated as the elliptical distance defined by the morphological parameters of these galaxies, derived by SEXTRACTOR. The less massive galaxies of the cluster were masked to reduce the contamination of their different stellar populations at a given radius. This radial distance was logarithmic spaced in eight bins, from 0 to 120 kpc. We illustrate the different bins in Fig. 1.

The reason to choose the above parameters, and their binning, is to characterize the stellar populations of the cluster properly, i.e. averaging zones with similar properties. This allows us to describe the cluster from its inner parts (brighter magnitudes, higher densities) to its outer parts (fainter magnitudes, lower densities) in a consistent way. On doing this, the comparison of the ICL properties with those from the cluster galaxies is direct and homogeneous. Consequently, we will infer the properties of the ICL and cluster galaxies based on their relative differences.

In Fig. 1, the three color-color diagrams based on the μ_J , $\log(\rho)$ and R maps of the cluster are shown (left panels). A grid of Bruzual & Charlot (2003) models based on a Salpeter IMF for single stellar populations is also plotted. Each of the points of the grid is flagged with its corresponding age and metallicity. For illustration, in the right panels, the color-coded bins of the three parameters are drawn over an image of the cluster in the F160W band.

3. RESULTS

3.1. Color-color diagrams

The left panels of Fig. 1 show the color-color diagrams for each parameter used to characterize the cluster light, i.e. μ_J , $\log(\rho)$ and R . Each data point on the color-color diagram corresponds to the average restframe $g - r$ and $i - J$ color values of the spatial regions drawn in the cluster maps plotted in the right panels. The errors in the $g - r$ and $i - J$ colors are derived from bootstrapping simulations. These simulations consist of 3000 realizations randomly choosing half of the pixels in each bin and calculating their mean colors. The errors represent the scatter of the distributions of the means. These errors account for both the intrinsic scatter of the cluster's stellar populations and the photometric errors. In addition, this bootstrapping technique could also account for local variations in the flat-field of the images.

For all the color-color diagrams, a continuous bluing of both $g - r$ and $i - J$ colors is clearly seen. Therefore, the stellar populations of the cluster (galaxies and ICL) become gradually bluer when moving away from the centers of the galaxies (i.e., towards fainter luminosities and lower densities). According to the values of age and metallicity indicated by the grid of models, this gradient in colors is compatible with a gradient in metallicity, from a supersolar metallicity to a little subsolar, and also a slight gradient in age (see next subsection). It is worth noting a slightly discrepant point ($\lesssim 3\sigma$) at ~ 5 kpc in the radial distance plot. We think this discrepant point is due to a combination of low statistics and mixing of different stellar populations at that radius.

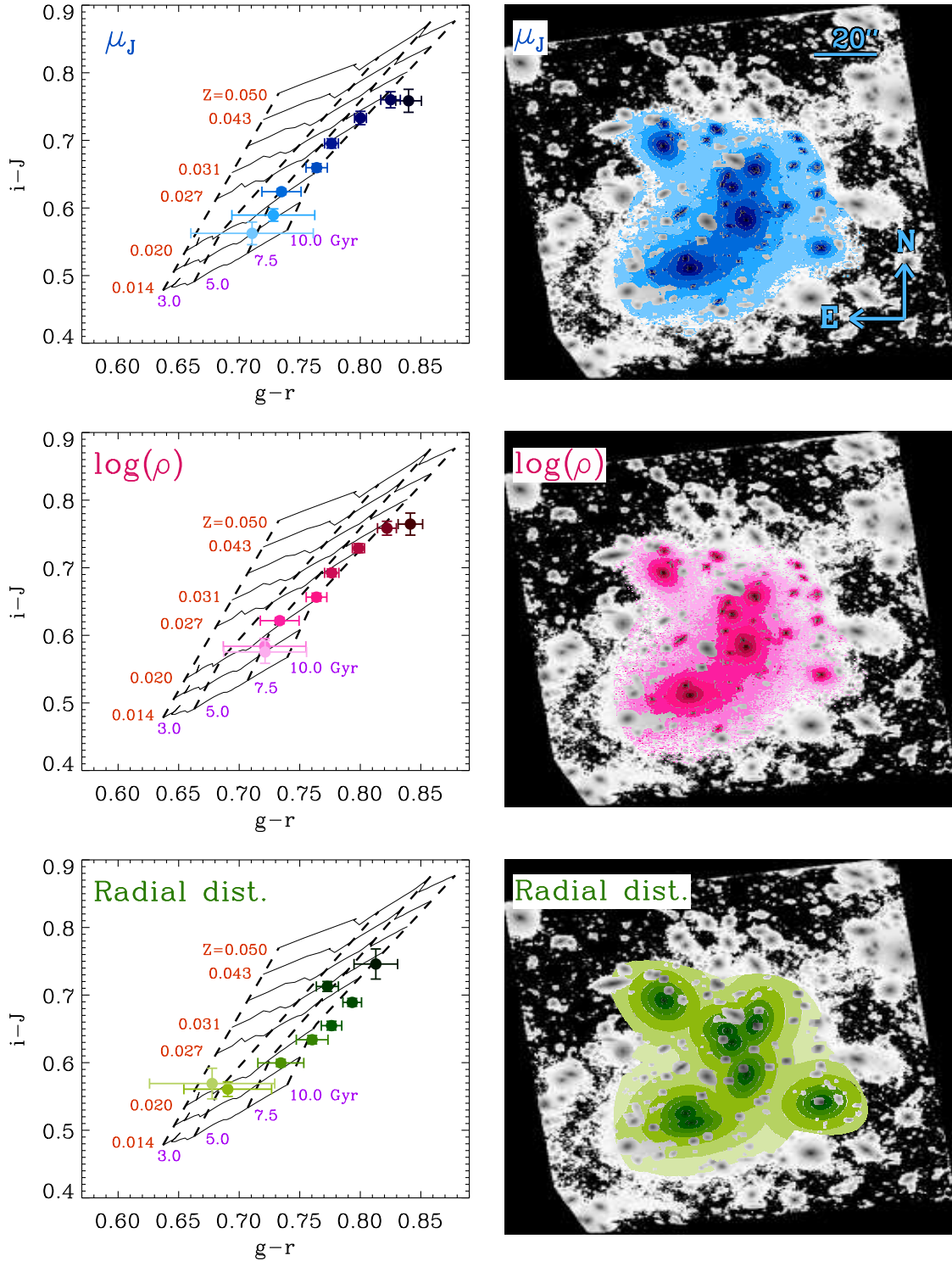


FIG. 1.— Left panels show the $i - J$ vs. $g - r$ diagrams for three different parameters: μ_J (blue), $\log(\rho)$ (pink) and R (green) used to characterize the different spatial regions where the light of the cluster is distributed. Overplotted is a color grid prediction based on Bruzual & Charlot (2003) models using a Salpeter IMF for single stellar populations. Right panels show the image of the cluster in the F160W filter and over-plotted are the different spatial regions in which the colors are measured. The spatial regions are coded from the inner parts of the cluster (darker color) to the outer parts (lighter color).

Sources of noise	Affecting	Relative impact	Addressed in Section
Time variable sky background	Few exposures in the IR	Modeled during the reduction process	2
Flat-field accuracy	All images	< 1% across the detector	2 & 3
PSF uncertainties	All images	$g - r < 0.03$ & $i - J < 0.02$	Appendix
Background estimation	All images	No gradients. Errors of < 5%	2.1.1

TABLE 1
SUMMARY OF THE SOURCES OF NOISE/UNCERTAINTY PRESENT IN OUR ANALYSIS.

A potential source of concern in our color determination is the effect of the PSF on the color distribution. Consequently, it is important to quantify a possible contamination of the colors in the outer regions of the cluster due to the scattered light produced by the different band PSFs. We have quantified this effect by modeling the effect of the different band PSFs in a model galaxy without and with a modeled ICL component. This is described in the Appendix. We find that the effect of the PSF both for the $g - r$ and $i - J$ colors is small (less than 0.03 and 0.02 mag, respectively, at the region of the ICL, i.e. $R > 50$ kpc) and less than 0.01 mag when adding an ICL component. Moreover, if any, the PSF effect on the color profile tends to redden the color. As we are observing a continuous bluing of the color radial profile, we conclude that the effect of the PSF plays a minor role in our analysis.

3.2. Age and metallicity gradients

To quantify the changes of the stellar populations across the galaxy cluster, we have computed the age and metallicity of the stellar populations based on their rest-frame $g - r$ and $i - J$ colors. Within each spatial bin, we measure the age and the metallicity of each pixel corresponding to their $g - r$ and $i - J$ colors. Then, we estimate the corresponding mean age and metallicity. The errors in age and metallicity were also drawn from the bootstrapping simulations used to derive the color errors. The gradients of age (upper panels) and metallicity (bottom panels) for each of the parameters are shown in Fig. 2. The colors, ages and metallicities for the three parameters are listed in Table 2.

In Fig. 2, tentatively, we marked in orange the region corresponding to the ICL component. Observationally, the exact definition of which part of the cluster light describes the ICL is ill-defined. There have been many different attempts to label the ICL region using criteria as the surface brightness or the radial distance. For instance, Zibetti et al. (2005) defined the ICL as the light with $\mu_r > 25.0$ mag/arcsec² whereas Toledo et al. (2011) used $R > 50$ kpc (see also Gonzalez et al. 2005). For each of the parameters used, we have defined the ICL region as the region with either restframe $\mu_J > 24$ mag/arcsec², $\log(\rho) < 1.2$ or $R > 50$ kpc. The μ_J limit defining the ICL region is based on the Zibetti et al. definition and was calculated using $i - J = 0.6$ (see Fig. 1) and $r - i = 0.4$ (Vazdekis et al. 2012, for solar metallicity and ~ 7 Gyr) while the $\log(\rho)$ limit is calculated using the above μ_J limit and the color $i - J = 0.6$. These values are inserted into equation 1 in Bakos et al. (2008) with the mass to light ratio in the J -band given by Vazdekis et al. (2012) models for the corresponding age (~ 7 Gyr) and metallicity ($Z \sim 0.018$) of the ICL region.

According to Fig. 2, the metallicity within the cluster is continuously decreasing from supersolar ($Z = 0.028 \pm 0.003$) in the central part of the main galaxies to solar ($Z = 0.018 \pm 0.007$) in the ICL region. The ICL metallicity is similar to that found in the stellar halo of nearby massive galaxies (Coccatto et al. 2010; Roediger et al. 2011; Greene et al. 2012; Montes et al. 2014). The stellar population ages show a slight negative gradient towards the outskirts. This gradient is compatible with what is found for the giant elliptical galaxy M87 (Liu et al. 2005; Montes et al. 2014), the elliptical

galaxies in Roediger et al. (2011) and for some galaxies in Greene et al. (2012).

4. DISCUSSION

State-of-the-art semianalytical models of galaxy formation (i.e. Contini et al. 2014) suggest that the origin of the ICL is the result of the disruption and tidal stripping of massive ($10^{10-11} M_\odot$) satellite galaxies infalling in the cluster potential (see also Purcell et al. 2007; Murante et al. 2007; Martel et al. 2012). The largest contribution of these massive satellites to the ICL is understood due to the stronger effect of dynamical friction on these galaxies orbiting the cluster compared to less massive satellites. If this theoretical scenario is correct, we would expect that the mean metallicity of the ICL would be slightly subsolar $Z \sim 0.009 - 0.014$ (Contini et al. 2014, corresponding to the typical metallicities of the galaxies described above). Here we find that the mean metallicity of the ICL in our cluster is solar ($Z = 0.018 \pm 0.007$), but still in agreement with the theoretical predictions. Using the mass-metallicity relation (Gallazzi et al. 2005), the derived ICL metallicity corresponds to the metallicities of galaxies with $M_\star \sim 3 \times 10^{10} M_\odot$. This mass is only a factor of two different to that of the Milky Way and the metallicity is similar ($6.43 \pm 0.63 \times 10^{10} M_\odot$, McMillan 2014; $Z \approx 0.02 = Z_\odot$, Rix & Bovy 2013). Therefore, the ICL of Abell 2744 can be understood as mainly produced by the disruption of galaxies with similar stellar properties as the Milky Way.

Many theoretical works (e.g. Willman et al. 2004; Monaco et al. 2006; Murante et al. 2007) find that the majority of the ICL formed at $z < 1$. According to Contini et al. (2014), it is only since $z = 0.4 - 0.5$ that 50% of the ICL of present-day clusters is in place. We find that the ICL age of Abell 2744 is younger (6 ± 3 Gyr) than the age of the most massive ($M_\star \gtrsim 10^{11} M_\odot$) galaxies of the cluster. This is consistent with the idea that the galaxies that mostly contributed to the ICL were producing stars during a larger period of time than the most massive galaxies of the cluster. This could happen if the satellite galaxies orbiting the cluster were forming stars until their star formation ceased due to ram pressure stripping of their gas content (e.g. Boselli et al. 2009; Chung et al. 2009). Later on, with their star formation stopped, the stellar populations of these satellite galaxies could be stripped from their progenitors and started to contribute to the ICL. However, it is not straightforward to say exactly when the ICL in Abell 2744 was produced. Nonetheless, we can speculate on the basis of the difference between the age of the most massive galaxies and the one derived for the ICL⁶. If we assume that the stellar populations of the most massive galaxies were formed at $z \sim 2 - 3$ (i.e. $\sim 10 - 11$ Gyr ago), then the ICL of Abell 2744 is compatible with being assembled at $z < 1$.

The restframe optical color of the ICL of Abell 2744 ($g - r \sim 0.68 \pm 0.04$) is consistent with the results of Krick et al. (2007) for the ICL of the same cluster ($V - r = 1.0 \pm 0.8$). We also compare the color of the ICL of Abell 2744 with the ICL colors available for

⁶ We do not use the absolute value of the ages of the stellar populations as it is well known that these values are more prone to errors than their relative differences (e.g. Vazdekis et al. 2001).

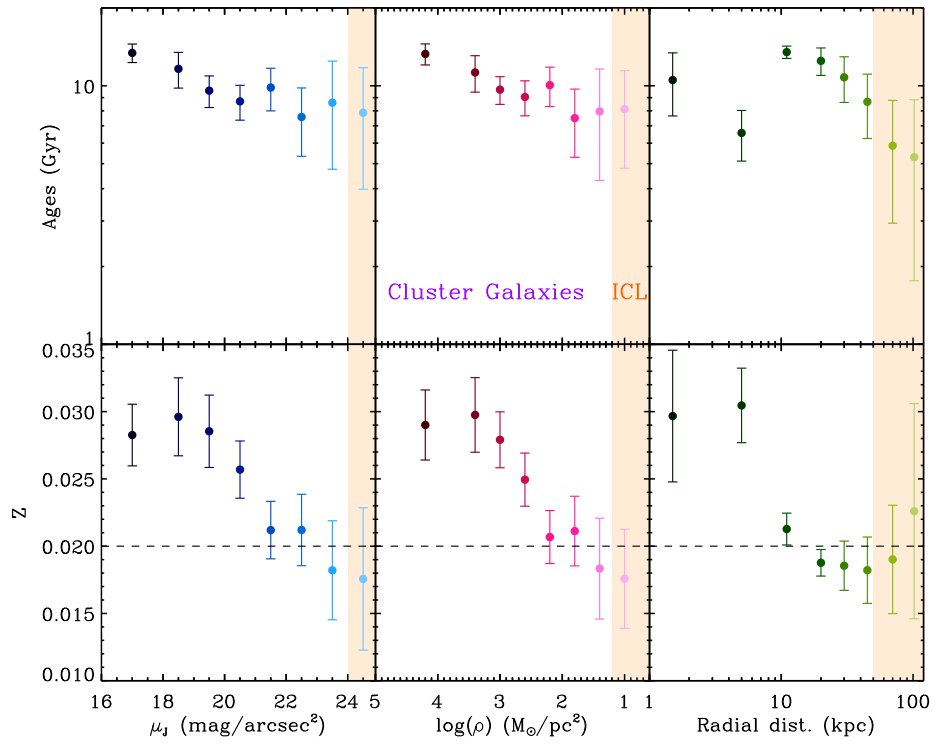


FIG. 2.— Gradients of age and metallicity as a function of μ_J , $\log(\rho)$ and R . The regions corresponding to the cluster galaxies (purple) and the ICL (orange) are labeled. The dashed line indicates the solar metallicity.

other clusters. As mentioned before, there are few studies regarding the properties of the ICL, even colors. We warn the reader that the clusters studied in the literature have different masses and redshifts making the comparison of such properties not straightforward. The derived color for the ICL of Abell 2744 is in agreement with the colors derived for various tidal features in the Virgo Cluster ($B - V \sim 0.75$, Rudick et al. 2010) and the outskirts of M87 ($g - r \approx 0.72$, Chen et al. 2010, priv. comm.). Covone et al. (2006) also found blue colors ($B - V \sim 1.0 \pm 0.5$) for two diffuse features in the cluster Abell 2667 at $z = 0.233$ compared to the colors of the most massive galaxies ($B - V \sim 1.5$), although there is a hint of a redder $V - I$ color for the ICL ($V - I \sim 1.0 \pm 0.3$ for the ICL, $V - I \sim 0.7$ for the galaxies).

Finally, another aspect of the ICL that can be directly compared with the theoretical predictions is the fraction of stellar mass of the galaxy cluster that is contained within this component. As we mentioned earlier, the precise definition of what is exactly ICL is observationally ill-defined. Here we have used up to three independent parameters to quantify the spatial region corresponding to the ICL: $24 < \mu_J < 25$ mag/arcsec², $0.8 < \log(\rho) < 1.2$ and $50 < R < 120$ kpc. The amount of stellar mass in the spatial regions defined by those constraints were derived as follows. For $\log(\rho)$ the derivation of the mass was straightforward, while for μ_J and the radial distance we used Equation 1 and the corresponding mass to light ratio in the J -band for the age and metallicity of the ICL region (see Fig. 2). The total mass of the cluster, including the ICL region, was obtained similarly but using all the spatial region covered by the light of the cluster explored in this work (i.e. $\sim 400 \times 400$ kpc around its core). The amount of total stellar mass in this region of the cluster is: $7.5 \times 10^{12} M_\odot$ ($\mu_J < 25$ mag/arcsec²), $7.9 \times 10^{12} M_\odot$ ($\log \rho > 0.8$) and $4.2 \times 10^{12} M_\odot$ ($R < 120$ kpc, using our definition of radial distance to the centers of the most massive galaxies of the cluster). The ICL mass fractions we got are: 5.1% for μ_J , 4.0% for $\log(\rho)$ and 10.4% for the radial distance. These ICL mass fractions correspond to the mass contained in 4 – 6 Milky Way-type galaxies. Note, however,

that these fractions are lower limits to the global contribution of the ICL to the total stellar mass of the cluster. This is due to the fact that we are not considering the whole cluster (but only $\sim 400 \times 400$ kpc around its core) and we are also limited by the depth of the optical bands (particularly for estimating $\log(\rho)$ based on the $r - z$ color). How our numbers compare with the theoretical expectations? Simulations predict that the fraction of mass in the ICL of present-day galaxy clusters should be around 10%-40% (Contini et al. 2014). At the redshift of our cluster, $z = 0.3$, the fraction of stellar mass in the ICL is expected to be around 60% of today's value. Consequently, we assume that the fraction of mass in a cluster as Abell 2744 should be between 6%-24%. Taking into account that our stellar mass estimates are lower limits, our numbers are in good agreement with theoretical expectations. The simulations are also in nice agreement with other stellar mass fractions measured in other clusters (10%-20%; Feldmeier et al. 2004; Covone et al. 2006; Krick et al. 2006, 2007). Over and over, it seems that the theoretical predictions are reproducing well the observations presented in this work and in other previous papers. We think this is an indication that we are starting to understand the general picture of how the ICL of the galaxy clusters form.

The results presented in this work show the extraordinary power of the Frontier Fields survey to address the origin and evolution of the ICL. Once this survey will be completed, it will be possible to explore the properties of the ICL in another 5 clusters in the redshift range 0.3 – 0.6; a period of time crucial to understand the formation of this elusive component of the galaxy clusters.

We thank the referee for constructive comments that helped to improve the original manuscript and the HST director and FF teams for their work to make these extraordinary data available. We also thank A. M. Koekemoer for his useful comments in the HFF image reduction process. This research has been supported by the Spanish Ministerio de Economía y Competitividad (MINECO; grant AYA2010-21322-C03-02).

REFERENCES

- Anders, P., Bissantz, N., Fritze-v. Alvensleben, U. & de Grijs, R. 2004, MNRAS, 347, 196
- Arnaboldi, M. & Gerhard, O. 2010, Highlights of Astronomy, 15, 97
- Bakos, J., Trujillo, I. & Pohlen, M. 2008, ApJ, 683, L103
- Bell, E. F., McIntosh, D. H., Katz, N. & Weinberg, M. D. 2003, ApJS, 149, 289
- Boschin, W., Girardi, M., Spolaor, M. & Barrena, R. 2006, A&A, 449, 461
- Boselli, A., Boissier, S., Cortese, L. & Gavazzi, G. 2009, Astronomische Nachrichten, 330, 904
- Bruzual, G. & Charlot, S. 2003, MNRAS, 344, 1000
- Cardelli, J. A., Clayton, G. C. & Mathis, J. S. 1989, ApJ, 345, 245
- Cebrián, M. & Trujillo, I. 2014, arXiv:1404.7135
- Chen, C.-W., Côté, P. & West, A. A. 2010, ApJS, 191, 1
- Chung, A., van Gorkom, J. H., Kenney, J. D. P., et al. 2009, AJ, 138, 1741
- Cocato, L., Gerhard, O. & Arnaboldi, M. 2010, MNRAS, L26
- Conroy, C., Wechsler, R. H. & Kravtsov, A. V. 2007, ApJ, 668, 826
- Contini, E., De Lucia, G., Villalobos, Á. & Borgani, S. 2014, MNRAS, 437, 3787
- Covone, G., Adami, C., Durret, F., et al. 2006, A&A, 460, 381
- de Vaucouleurs, G. 1948, Annales d'Astrophysique, 11, 247
- Durrell, P. R., Ciardullo, R., Feldmeier, J. J., et al. 2002, ApJ, 570, 119
- Feldmeier, J. J., Mihos, J. C., Morrison, H. L., et al. 2004 ApJ, 609, 617
- Ferreras, I., Trujillo, I., Mármol-Queraltó, E. 2014, arXiv:1312.5317
- Gallazzi, A., Charlot, S., Brinchmann, et al. 2005, MNRAS, 362, 41
- Gonzalez, A. H., Zabludoff, A. I. & Zaritsky, D., 2005, ApJ, 666, 147
- Gonzalez, A. H., Zaritsky, D. & Zabludoff, A. I., 2007 ApJ, 666, 147
- Gregg, M. D. & West, M. J., 1998, Nature, 396, 549
- Greene, J. E., Murphy, J. D., Comerford, J. M., et al. 2012, ApJ, 750, 32
- Hopkins, P. F., Bundy, K., Murray, N., et al. 2009, MNRAS, 398, 898

μ_J (mag/arcsec ²)				
Bin	$g-r$	$i-J$	Age (Gyr)	Z
16-18	0.840 ± 0.011	0.759 ± 0.017	13.401 ± 1.102	0.028 ± 0.002
18-19	0.825 ± 0.008	0.760 ± 0.012	11.631 ± 1.835	0.030 ± 0.003
19-20	0.800 ± 0.005	0.733 ± 0.010	9.579 ± 1.339	0.029 ± 0.003
20-21	0.776 ± 0.006	0.695 ± 0.007	8.703 ± 1.341	0.026 ± 0.002
21-22	0.764 ± 0.009	0.660 ± 0.006	9.846 ± 1.847	0.021 ± 0.002
22-23	0.735 ± 0.016	0.624 ± 0.004	7.574 ± 2.238	0.021 ± 0.003
23-24	0.728 ± 0.034	0.590 ± 0.009	8.605 ± 3.850	0.018 ± 0.004
24-25	0.711 ± 0.051	0.562 ± 0.017	7.866 ± 3.884	0.018 ± 0.005
log($\rho(M_\odot/pc^2)$)				
4.8-3.6	0.841 ± 0.010	0.765 ± 0.016	13.281 ± 1.242	0.029 ± 0.003
3.6-3.2	0.822 ± 0.008	0.758 ± 0.010	11.262 ± 1.812	0.030 ± 0.003
3.2-2.8	0.799 ± 0.005	0.729 ± 0.007	9.661 ± 1.187	0.028 ± 0.002
2.8-2.4	0.776 ± 0.006	0.692 ± 0.006	9.052 ± 1.400	0.025 ± 0.002
2.4-2.0	0.764 ± 0.009	0.656 ± 0.006	10.060 ± 1.746	0.021 ± 0.002
2.0-1.6	0.733 ± 0.016	0.622 ± 0.005	7.499 ± 2.210	0.021 ± 0.003
1.6-1.2	0.721 ± 0.034	0.584 ± 0.012	7.959 ± 3.654	0.018 ± 0.004
1.2-0.8	0.721 ± 0.034	0.575 ± 0.017	8.118 ± 3.318	0.018 ± 0.004
Radial distance (kpc)				
0- 3	0.813 ± 0.018	0.746 ± 0.022	10.528 ± 2.882	0.030 ± 0.005
3- 7	0.773 ± 0.009	0.713 ± 0.007	6.571 ± 1.458	0.030 ± 0.003
7-15	0.793 ± 0.008	0.689 ± 0.006	13.500 ± 0.740	0.021 ± 0.001
15-25	0.776 ± 0.008	0.655 ± 0.007	12.488 ± 1.522	0.019 ± 0.001
25-35	0.760 ± 0.013	0.634 ± 0.006	10.784 ± 2.161	0.019 ± 0.002
35-55	0.734 ± 0.019	0.600 ± 0.005	8.674 ± 2.421	0.018 ± 0.002
55-85	0.691 ± 0.036	0.561 ± 0.011	5.864 ± 2.922	0.019 ± 0.004
85-120	0.678 ± 0.052	0.569 ± 0.023	5.298 ± 3.536	0.023 ± 0.008

TABLE 2

Krick, J. E. & Bernstein, R. A. 2007, AJ, 134, 168	Roediger, J. C., Courteau, S., MacArthur, L. A. & McDonald, M. 2011, MNRAS, 416, 1996
Laporte, N., Streblyanska, A., Clement, B., et al. 2014, A&A, 562, L8	Rudick, C. S., Mihos, J. C. & McBride, C. 2006, ApJ, 648, 936
Liu, Y., Zhou, X., Ma, J., et al. 2005, AJ, 129, 2628	Rudick, C. S., Mihos, J. C., Harding, P., et al. 2010, ApJ, 720, 569
McMillan, P. J. 2014, MNRAS, 414, 2446	Salpeter, E. E. 1955, ApJ, 121, 161
Martel, H., Barai, P. & Brito, W. 2012, ApJ, 757, 48	Schlafly, E. F. & Finkbeiner, D. P. 2011, ApJ, 737, 103
Mihos, J. C., Harding, P., Feldmeier, J. & Morrison, H. 2005, ApJ, 631, L41	Shen, S., Mo, H. J., White, S. D. M., et al. 2003, MNRAS, 343, 978
Monaco, P., Murante, G., Borgani, S. & Fontanot, F. 2006, ApJ, 652, L89	Toledo, I., Melnick, J., Selman, F. et al. 2011, MNRAS, 414, 602
Montes, M., Trujillo, I., Prieto, M. A. & Acosta-Pulido, J. A. 2014, MNRAS, 439, 990	Vazdekis, A., Salaris, M., Arimoto, N. & Rose, J. A. 2001, ApJ, 549, 274
Murante, G., Arnaboldi, M., Gerhard, O., et al. 2004, ApJ, 607, L83	Vazdekis, A., Ricciardelli, E., Cenarro, A. J., et al. 2012, MNRAS, 424, 157
Murante, G., Giovalli, M., Gerhard, O., et al. 2007, MNRAS, 377, 2	Williams, B. F., Ciardullo, R., Durrell, P. R., et al. 2007, ApJ, 656, 756
Oser, L., Naab, T., Ostriker, J. P., et al. 2012, ApJ, 744, 63	Willman, B., Governato, F., Wadsley, J. & Quinn, T. 2004, MNRAS, 355, 159
Owers, M. S., Randall, S. W., Nulsen, P. E. J., et al. 2011, ApJ, 728, 27	Zibetti, S., White, S. D. M., Schneider, D. P. & Brinkmann, J. 2005, MNRAS, 358, 949

APPENDIX

EFFECT OF THE PSF

In order to estimate a possible contamination of the colors in the outer regions of the cluster due to the scattered light produced by the different band PSFs, we run the following tests. We have created an artificial galaxy with an effective radius of 5 kpc. This value is typical of galaxies with $10^{11} M_\odot$ (see e.g. Shen et al. 2003; Cebrián & Trujillo 2014). The mock galaxy follows a de Vaucouleurs $r^{1/4}$ profile (de Vaucouleurs 1948). The surface brightness profile of the simulated galaxy was convolved with the different HST PSFs. As we are interested on exploring the effects cause by the PSF wings in the outer region of our profiles, our PSFs were retrieved from the HST PSF modeling software TINYTIM. We retrieved from the TINYTIM webpage the largest PSF available for each band ⁷. This allows us to use PSFs that extends at least over 12.5'' (i.e. 55 kpc at the cluster redshift). We also simulated the effect of adding an ICL profile, an exponential profile with scale length of 18 kpc and $\mu_J = 24.5$ mag/arcsec² at $R = 50$ kpc.

The original model profiles and the convolved PSF models are shown in Fig. 3 (without ICL) and 4 (with ICL). As input colors for the model profiles we have used $g-r = 0.85$ and $i-J = 0.75$, which are typical colors of the inner regions of the galaxies. In Fig. 3, we find that the effect of the different PSFs and their wings in the constructed radial colors is less than 0.03 and 0.02 mag in the $g-r$ and $i-J$ colors, respectively, at the region of the ICL ($R > 50$ kpc). However, in Fig. 4 where the ICL is included, we find that the smoother profile of the ICL diminishes the effect of the PSF and the colors differ in less than 0.01 mag from the simulations. We warn the reader that these are the results of a simple simulation. We only consider the effect of one galaxy and the ICL region could be affected by the scattered light of other galaxies of the cluster. Consequently, the only purpose of these simulations is to provide a hint about how relevant could be the PSF effect on the ICL region.

⁷ Ideally, we would like to base our analysis using an empirical PSF. Unfortunately, there are not bright, isolated stars in the field

of view to conduct such exercise.

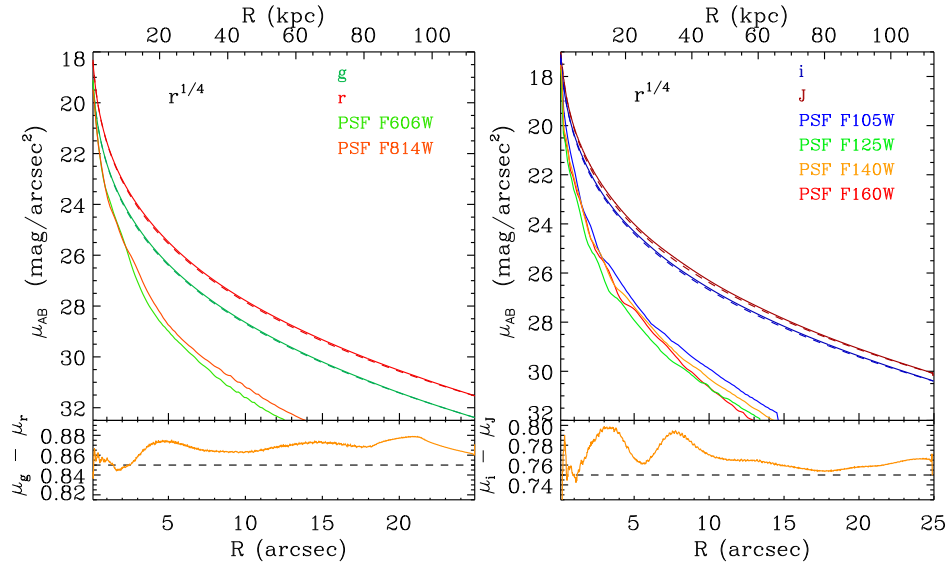


FIG. 3.— Upper panels: Surface brightness profiles of the models (dashed lines) and the convolved models (solid lines) for the ACS (left hand panel) and WFC3 (right hand panel) filters used in the analysis. The PSF profiles in all the observed used bands are also shown. The bottom panels show the effect of the PSF in the restframe colors: $g - r$ (left) and $i - J$ (right). The input model colors are indicated with dashed lines.

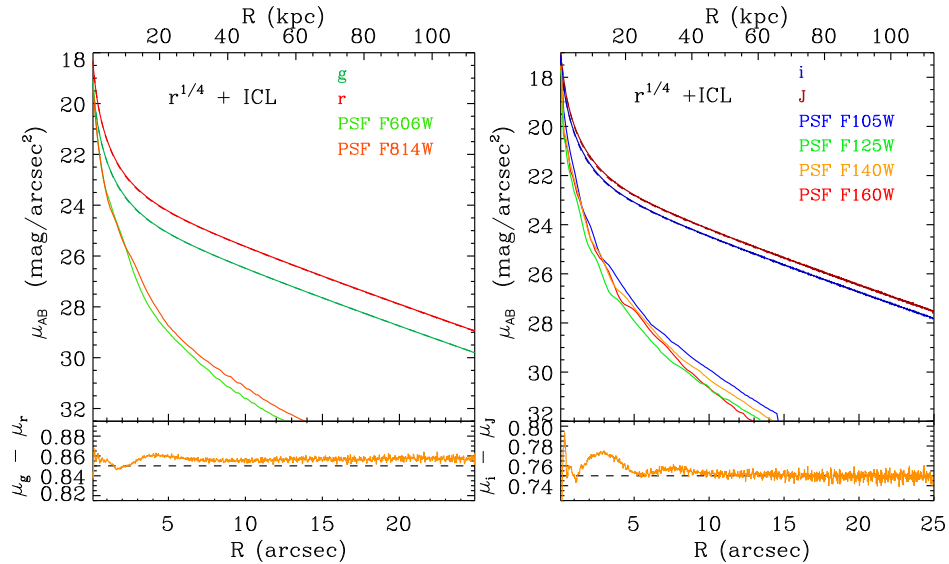


FIG. 4.— Same as in Fig 3 but adding an ICL component of scale length 18 kpc and $\mu_J = 24.5 \text{ mag/arcsec}^2$ at $R = 50 \text{ kpc}$.